Chapter 3

SELF-OPTIMIZING PHOTOELECTROCHEMICAL GROWTH OF NANOPATTERNED SE-TE FILMS IN RESPONSE TO THE SPECTRAL DISTRIBUTION OF INCIDENT ILLUMINATION

3.1 Introduction

In this chapter, we describe the relationship between the morphologies of photoelectrodeposited Se-Te films and the spectral profiles of the illumination utilized during the growth of the films. Deposition was performed in the presence of an array of narrowband, broadband, and multi-modal illumination profiles, respectively, to determine the morphology produced by changes in the properties of the optical excitation. Fourier analysis was utilized to provide a quantitative description of the patterns, and the patterns were accurately reproduced by computational modeling and simulation of the light-material interactions during growth of the films.

3.2 Results and Discussion
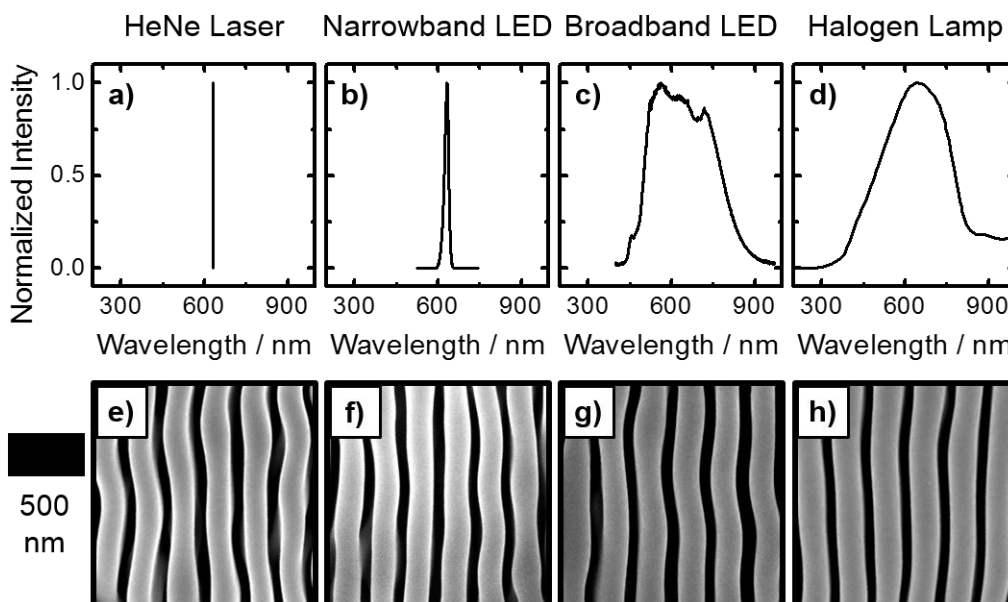
Figure 3.1. Effect of the spectral bandwidth of vertically polarized illumination sources on the morphology of photoelectrodeposited Se-Te films. (a)-(d) Spectral profiles for indicated sources. (e)-(h) Corresponding scanning electron micrographs representative of the resulting photoelectrodeposited films.

Se-Te photoelectrodeposits produced by illumination with polarized, narrowband coherent or incoherent light between $450 < \lambda < 950$ nm form lamellae that are aligned along the optical polarization direction, with a periodicity proportional to the incident optical wavelength. Figure 3.1(a)-(d) presents spectral profiles of four light sources that had very similar intensity-weighted average wavelengths (λ_{avg}) but had very different spectral bandwidths: a HeNe laser with $\lambda_{avg} = 633$ nm and a bandwidth (full-width at half-max, FWHM) << 1 nm; a narrowband light-emitting diode (LED) with $\lambda_{avg} = 630$ nm and FWHM = 18 nm; a broadband LED with $\lambda_{avg} = 646$ nm and FWHM = 283 nm; and a tungsten-halogen lamp with $\lambda_{avg} = 640$ and FWHM = 420

nm. Figure 3.1(e)-(h) presents representative scanning-electron micrographs (SEMs) of photoelectrodeposits generated by the potentiostatic electrochemical reduction of SeO_2 and TeO_2 under illumination with each separate, vertically polarized light source. The Se-Te films exhibited mutually similar morphologies regardless of which illumination source was utilized (Figure 3.1). These morphologies are similar to ripple patterns that are generated using laser surface processing, known as laser-induced periodic surface structures (LIPSS).[64-66] However, formation of LIPSS requires coherent, highly monochromatic, and extremely intense (typically at kW cm^{-2} or MW cm^{-2} scales) laser excitation, whereas none of the illumination sources utilized in this investigation had all of these qualities.[67,68] Moreover, the broadband LED and halogen lamps produced light that was incoherent and highly polychromatic, with intensities on the order of mW cm^{-2}. Thus, it is apparent that a distinct mechanism must control the pattern formation in the system considered herein.
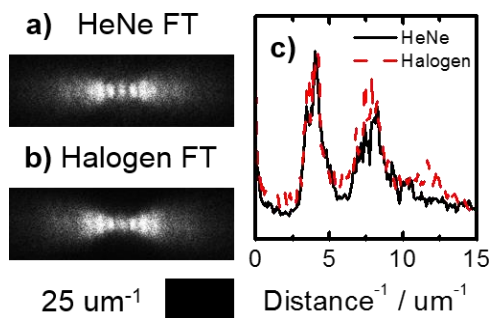
Figure 3.2. Fourier analysis of film morphologies generated with narrowband and broadband spectral distributions yielding a similar intensity-averaged wavelength. (a) and (b) Representative 2D Fourier transforms generated from SEMs of the films photoelectrodeposited using the indicated sources. (c) Fourier spectra generated by integrating the grayscale intensity along a narrow band starting at the center and extending out along the horizontal axis of the Fourier images presented in (a) and (b).

Figure 3.2(a) and (b) present two-dimensional Fourier transforms (2D FTs) of the SEM data of the photoelectrodeposited films using the HeNe laser and the tungsten-halogen lamp, respectively. A bright spot in a 2D FT corresponds to a periodic component in the SEM from which the 2D FT was derived. Moreover, in a 2D FT, the distance of any spot from the center indicates the frequency of the component, and the relative location indicates the direction of the periodicity. Thus the spots along the horizontal axes in Figure 3.2(a) and (b) are indicative of horizontal periodicity in the SEMs of the deposit morphologies. The similarity between the 2D FTs suggests that similar periodicities of the lamellar morphologies were generated with both the laser and the lamp. By integrating the grayscale intensity along a narrow band starting at the center and extending out along the horizontal axis of the 2D FT, a Fourier spectrum was generated to enable quantitative analysis of the data. Figure 3.2(c) presents Fourier spectra corresponding to the 2D FTs in Figure 3.2(a) and (b).

The extremely close agreement between the Fourier spectra describing the morphologies generated with the laser and lamp indicates a very similar periodic nature of these two morphologies despite a difference of several orders of magnitude between the bandwidths of the two sources.

The inverse of the lowest frequency maximum in each Fourier spectrum was equal to the lamellar periodicity (i.e. distance between identical points on two neighboring lamellae). The higher frequency maxima were integral multiples of the lowest maximum, and thus simply represent overtones of a fundamental frequency. The presence of overtones at higher frequencies is expected because the shapes of the lamellae are not perfectly described by a single sinusoidal function. The lack of any other components beyond a singular set of harmonics suggests that each morphology can be well-described by a single period. Thus despite the broadband source providing photons with widely differing excitation wavelengths, only a singular morphological periodicity was produced, exactly as is observed when a single periodicity results from a laser source that instead provides photons having only an extremely narrow distribution of wavelengths. Quantitatively, the real-space lamellar periodicity determined from the Fourier spectra was 245 ± 4 nm for deposits generated with the laser and 250 ± 3 nm for the lamp based on at least 5 independent measurements of each type of sample. Similar analysis of the deposits generated with LED sources resulted in a value of 244 ± 4 nm for the narrowband LED and 252 ± 8 nm for the broadband LED, again based on at least 5 independent measurements of each type of sample.
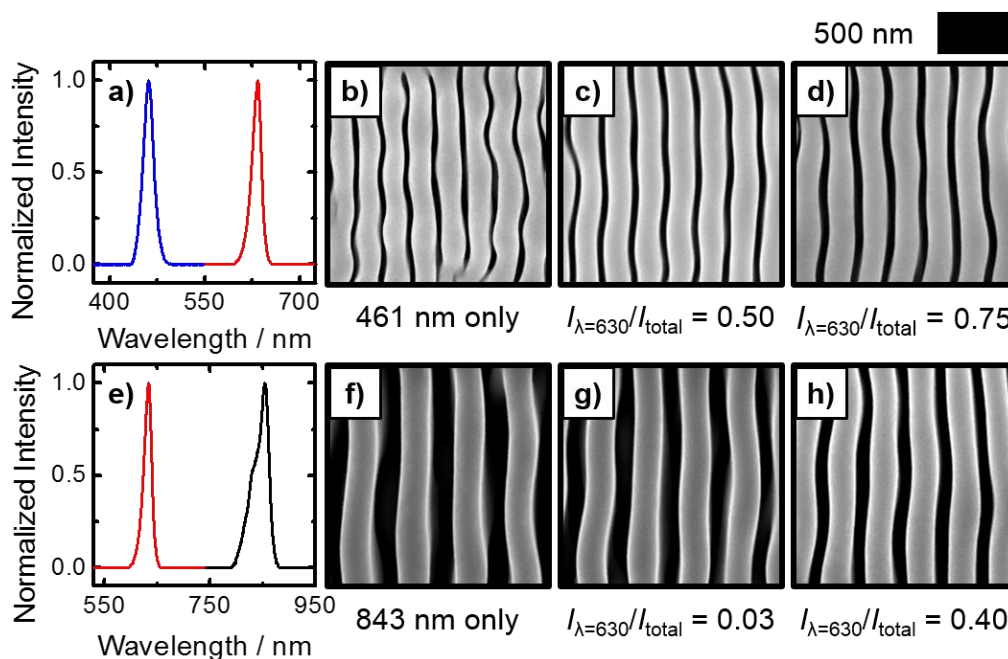
Figure 3.3. Effect of simultaneous illumination with two discrete narrowband sources on the morphology of the photoelectrodeposited Se-Te films. (a) Spectral profile of the illumination resulting from the combination of two narrowband LED sources with λ_{avg} values of 461 nm and 630 nm (at an arbitrary intensity ratio). (b)-(d) SEMs representative of the photoelectrodeposits resulting from illumination with a similar spectral profile as in (a) with the indicated intensity ratio between the two sources. (e)-(h) Same as (a)-(d), but with a source with a λ_{avg} value of 843 nm rather than 461 nm.

Collectively, the results obtained with the sources of varying bandwidths indicate that the lamellar periodicity is determined by an effective average source wavelength. This concept was investigated further by performing the photoelectrodeposition with spectral profiles that produced an intensity-weighted average spectral wavelength at a value at which the source had no actual intensity. Such profiles were obtained by simultaneously illuminating the sample with two narrowband LED sources. Figure 3.3(a) presents the spectral profile that resulted from illumination

with a narrowband LED with λ_{avg} = 630 nm in conjunction with illumination from another narrowband LED having λ_{avg} = 461 nm. Figure 3.3(b) presents a SEM of a deposit generated with only 461 nm illumination and Figure 3.3(c) and (d) presents SEMs of deposits generated with simultaneous illumination at 461 nm and 630 nm, as a function of the fraction of the total delivered intensity that was provided by each narrowband light source. The SEMs observed from a deposit generated using 461 nm illumination displayed a smaller lamellar periodicity than was observed for the corresponding deposit grown using 630 nm illumination. Deposits generated using illumination with both wavelengths appeared to display intermediate periodicities. Figure 3.3(e)-(f) presents analogous data, but with an LED having λ_{avg} = 843 nm rather than 461 nm. As noted in the experiment using 461 nm and 630 nm sources, the deposition under illumination with the longer wavelength source alone generated what appeared to be the largest periodicity, while deposits formed under illumination by both sources simultaneously resulted in lamellar periods intermediate between those observed for deposition with either source alone.
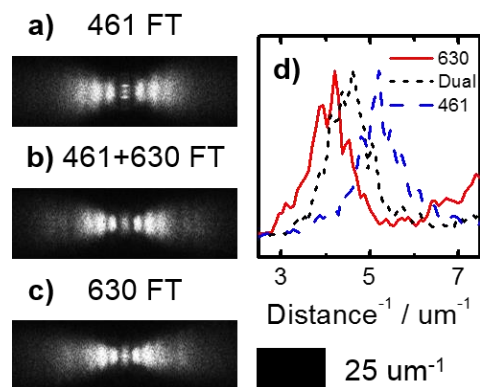
Figure 3.4. Fourier analysis of film morphologies generated with single and multimodal spectral distributions. Representative 2D Fourier transforms of SEMs of photoelectrodeposits generated using (a) a single narrowband source with a λ_{avg} value of 461 nm, (b) two narrowband sources with λ_{avg} values of 461 nm and 630 nm, and (c) a single narrowband source with a λ_{avg} value of 630 nm. (c) Fourier spectra generated by integrating the grayscale intensity along a narrow band starting at the center and extending out along the horizontal axis of the Fourier images presented in (a)-(c).

Fourier analysis was also used to analyze the periodicity of the patterns in the photoelectrodeposits grown using simultaneous illumination from two narrowband sources. Figure 3.4(a)-(c) presents 2D FTs of SEMs of deposits generated with illumination provided by the 461 nm source alone, the 461 and 630 nm sources together, and the 630 nm source alone. Each 2D FT displayed discrete bright spots along the horizontal axis, and the spacing of these spots was the greatest in the 2D FT of the 461 nm sample and smallest in the 2D FT of the 630 nm sample. The spacing in the 2D FT of the dual-wavelength sample was intermediate between the spacings for the 461 nm and 630 nm samples. In all three cases, the corresponding Fourier spectra generated from integration of these three 2D FTs revealed that the only observable components were a fundamental mode and corresponding overtones.

Figure 3.4(d) presents the corresponding Fourier spectra in the region of the fundamental. The fundamental peak in each spectrum was centered at a different value along the abscissa, and the center of the dual-wavelength peak was intermediate between the centers of both related single-wavelength peaks. Thus, under the conditions investigated, photoelectrochemical growth with two discrete narrowband sources resulted in a deposit that had only a single characteristic morphological period, and had no detectable beat frequencies in contrast to expectations based on simple interference.
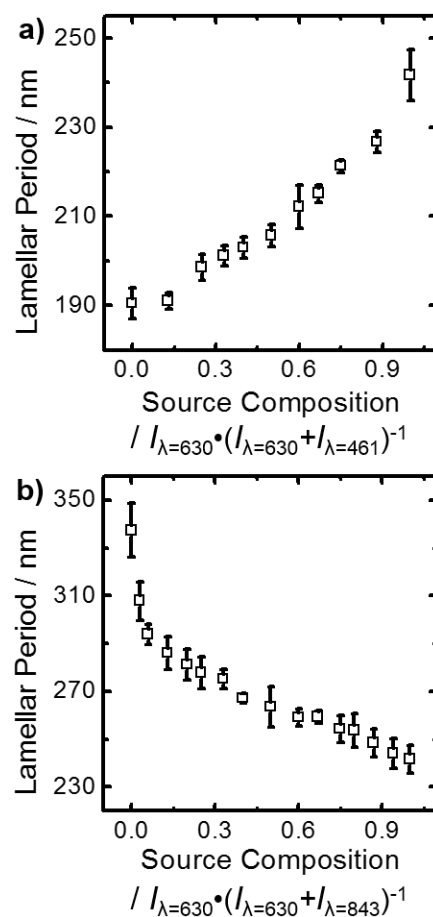
Figure 3.5. Photoelectrodeposit lamellar period as a function of the fraction of the total, two-source intensity provided by a 630 nm source utilized during growth.

Figure 3.5(a) presents a plot of the lamellar period derived from the 2D FTs of SEMs of photoelectrodeposits generated with simultaneous illumination at 461 nm and 630 nm as a function of the source composition. Figure 3.5(b) presents analogous data characteristic of photoelectrodeposits generated with 630 nm and 843 nm illumination. In both cases, the lamellar periods observed for photoelectrodeposits generated using simultaneous illumination with two different wavelengths were intermediate between those observed for photoelectrodeposits generated with either

one of the two constituent wavelengths alone. Also, in both cases, the lamellar period scaled monotonically between these limits as a function of source composition, in an inverse logistic-like curve. Such behavior has several implications. First, by utilization of two sources with differing wavelengths, a structure with any period between the limits defined by the periods observed for growth with either source alone can be generated simply by varying the relative intensity of the two sources. Second, under such conditions, the growth is sensitive to the characteristics of both sources, because the lamellar period reflected the engineered spectral profile of the illumination under every condition investigated. In fact, near the extremes of the source composition, wherein one source supplied the majority of the intensity, the lamellar period was generally the most sensitive to a change in source composition.
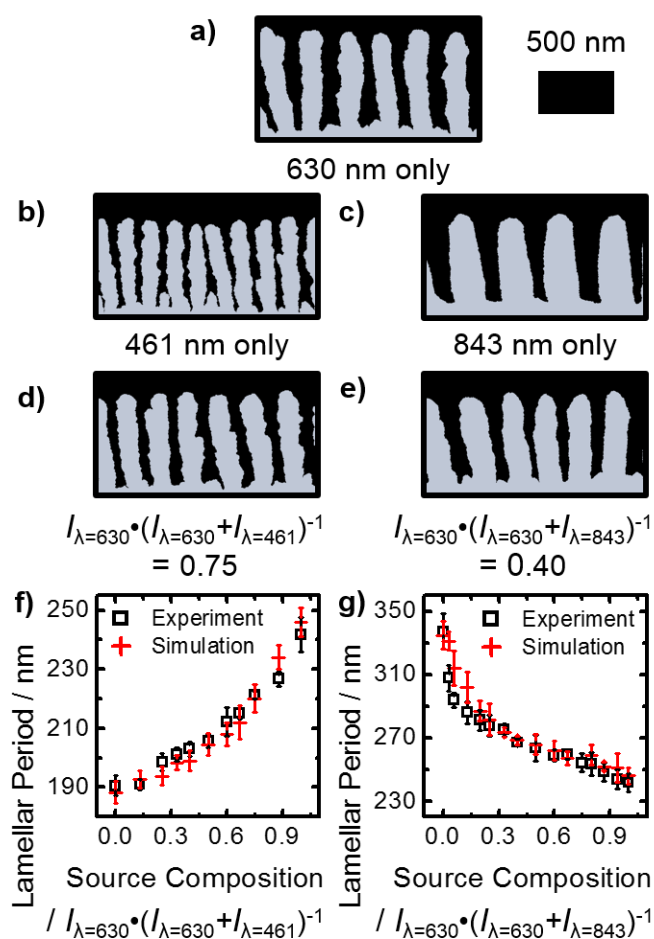
Figure 3.6. Computational growth modeling data representative of photoelectrodeposited Se-Te film morphologies generated using simultaneous illumination with two discrete narrowband sources. (a)-(e) 2D simulations of photoelectrodeposits generated with indicated illumination source(s). (f) and (g) Plots of lamellar period of the experimental and simulated photoelectrodeposit morphologies as a function of the fraction of the total, two-source intensity provided by a 630 nm source utilized during growth/modeling.

Modeling of the photoelectrochemical growth process was performed to determine if the morphologies observed for films generated using simultaneous illumination with narrowband sources evolved as a result of the fundamental light-matter interactions that occurred during the deposition. The two-step, iterative model

described in Chapter 1 was utilized wherein electromagnetic simulations were first used to calculate the local photocarrier-generation rates at the electrode/solution interface and then electrochemical addition of mass was simulated via a Monte Carlo method that utilized the local photocarrier-generation rate to weight the local probabilities of mass. Figure 3.6(a), (b), and (c), respectively, present 2D simulations (cross-sectional view) of the morphologies of photoelectrodeposits generated using illumination at 630 nm, 461 nm, and 843 nm alone. The morphological periodicity in each presented simulation was in good agreement with that observed experimentally (Figure 3.1(f), Figure 3.3(b) and (f)). Figure 3.6(d) and (e) present 2D simulations of the morphologies of photoelectrodeposits generated with illumination at 630 nm simultaneously with illumination at either 461 nm or 843 nm, respectively. In both cases, the simulated morphologies displayed periodicities that were intermediate between those observed in the simulations of morphologies generated under illumination with either of two sources alone. Moreover, the simulated morphologies were in good agreement with those observed experimentally (Figure 3.3(d) and (h)). Thus, the modeling and simulation agreed qualitatively with the experimental data.

The lamellar period in the simulated structures was derived from FT analysis, in an analogous fashion to analysis of the structures that were observed experimentally (Figure 3.2). Figure 3.6(f) presents the lamellar period of the morphologies of the simulated photoelectrodeposits, as well as the corresponding experimental morphologies, for growth under simultaneous illumination with 461 nm and 630 nm sources as a function of source composition. Figure 3.6(g) presents analogous data characteristic of simulations and photoelectrodeposits that were obtained by

simultaneous use of 630 nm and 843 nm illumination. The experimental and simulated values of the lamellar period matched quantitatively in both cases. Such quantitative agreement between the model and experiment indicates that any arbitrary illumination profile during growth encodes for a singular lamellar period. Additionally, the specific period appears spontaneously in the photoelectrodeposit due only to the interactions between the illumination and the evolving deposit during growth.

The generation of the highly anisotropic, periodic lamellar pattern is directly the result of highly differing rates of mass addition along the film surface. Specifically, to perpetuate the morphological asymmetry, the local growth rate must be greatest at the tip of the lamellar surface. Light absorption provides the driving force in the modeling for photoelectrochemical deposition, hence the success of the iterative growth model in reproducing the observations indicates that generation of the periodic lamellar pattern requires the absorption of light to be greatest in the tips of the lamellar structure and less than maximal in areas other than the tips of the structure. The experimental results and growth model also collectively indicated that a lamellar pattern having a single periodicity is always formed under the conditions investigated, regardless of the spectral profile of the illumination. Collectively, the experiments and simulations suggest that for a given illumination profile, the photoelectrodeposition process spontaneously self-selects the lamellar period that will maximize light absorption at the tips of the lamellar structures. A set of light-absorption simulations were performed considering an idealized lamellar structure to verify that the experimentally observed periods were those that maximized the anisotropy of the light absorption.
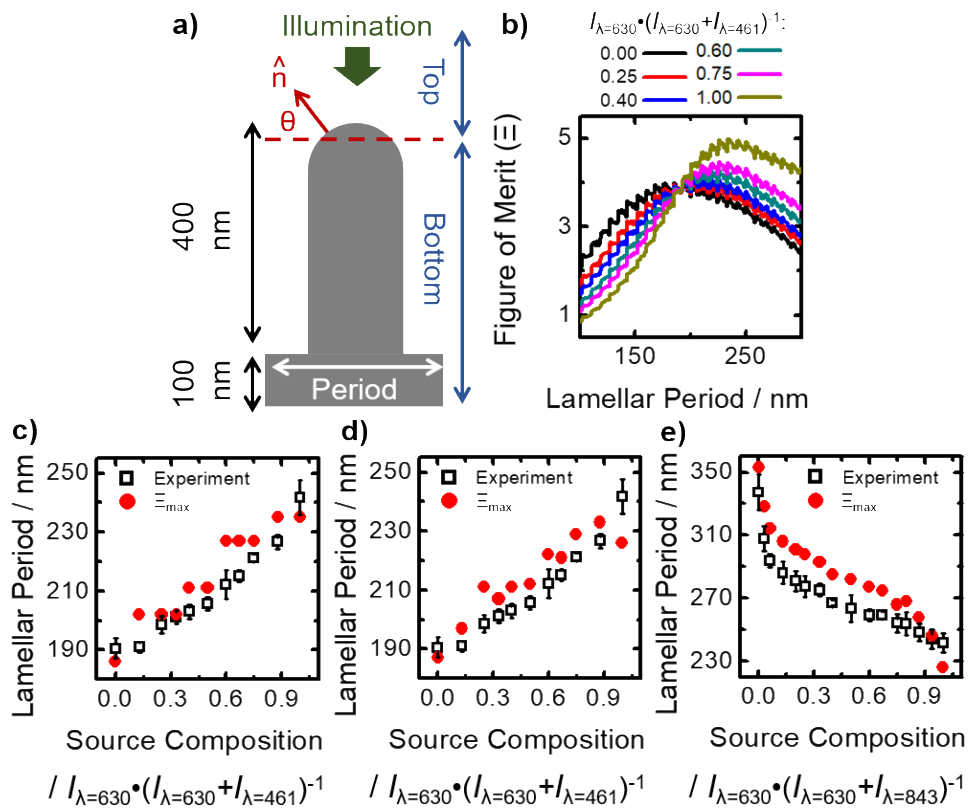
Figure 3.7. Computational analysis of light absorption anisotropy in idealized lamellar structures under simultaneous illumination with two discrete narrowband sources. (a) Diagram of the simulation area containing an idealized lamellar structure utilized for calculations of the spatial concentration of light absorption. The lamella was divided into top and bottom segments at the height at which the surface normal of the tip ($\hat{n}$) was at an angle $\theta = 45$ degrees from the horizontal. Plane-wave illumination was incident from the top of the structure, with a propagation oriented normal to the substrate. (b) Plots of figure of merit, Ξ, or light absorption in the top surface of the idealized structure normalized by that in the bottom, as a function of lamellar period for simultaneous illumination at 461 nm and 630 nm with the indicated source composition. (c) Plot of the experimentally observed lamellar period and the lamellar period which maximized Ξ as a function of the fraction of the total intensity provided by the 630 nm source utilized during growth/modeling. (d) and (e) Same as (c) but based on simulations utilizing a finer discretization of the lamellar structure.

Figure 3.7(a) provides a schematic for the simulation area that contained the idealized structure, consisting of a 400 nm tall lamella that had a hemispherical upper bound atop a 100 nm conformal layer of the electrodeposit. The width of structures in the simulations was set as the product of the lamellar period and the empirically derived filling fraction for the illumination condition under analysis (quantified by contrast-thresholding the same SEMs utilized for Fourier analysis). The illumination was simulated to be incident with a propagation vector parallel to the lamellar tip. Periodic boundary conditions were used to simulate an array of lamellae. The structure was considered as two segments, "top" and "bottom", with the boundary between the two segments located at the height at which the surface normal of the tip was 45 degrees from horizontal. A figure of merit, Ξ, was defined as the ratio of absorbed photons in the interfacial region of the top versus that of the bottom. A figure of merit, Ξ, was defined as the ratio of number of absorbed photons at the top solid/solution interface to the number of absorbed photons at the bottom solid/solution interface. The value of Ξ was thus proportional to the degree of light concentration in the top of the lamellar structure. Calculation of Ξ was limited to photons that were absorbed within 10 nm of the interface.

For a given illumination profile, Ξ was calculated over a series of lamellar periods ranging from 100 to 400 nm. Figure 3.7(b) illustrates the dependence of Ξ on the lamellar period for simultaneous illumination at 461 nm and 630 nm with several experimentally investigated source compositions. Each Ξ-curve had a single maximum, which shifted to a larger value of the lamellar period for illumination profiles as the 630 nm content of the illumination increased. Figure 3.7(c) presents a plot of the lamellar

period at Ξ_{max} for simulations involving simultaneous illumination at 461 nm and 630 nm, as a function of the source composition. The experimentally observed values are also presented in Figure 3.7(c). The stair-step shape of the Ξ-derived curve is an artifact that arose because the simulations considered the structure as many finite, but insufficiently small, units. Identical simulations that instead involved smaller units exceeded the available computational resources. Nevertheless, the values of the lamellar period that maximized Ξ matched semi-quantitatively with the analogous experimental values. To accommodate computational limitations while improving the accuracy of the model, Ξ was recalculated with simulations that utilized a finer discretization of the structure, but only was performed in a narrow range of lamellar periods near the previously observed maxima (using the coarser discretization), for every experimentally investigated source composition. Figure 3.7(d) presents the derived plot of the lamellar period at the new values of Ξ_{max}, along with the related experimental data. Figure 3.7(e) presents an analogous plot for simultaneous illumination with 630 nm and 843 nm. The lamellar periods that maximized Ξ followed the same trend with respect to source composition as the experimentally measured periods, and the two sets of values matched essentially quantitatively. The agreement between the experimental data and the simulations indicates that the observed photoelectrochemical growth spontaneously optimized the lamellar period in a way that maximized the anisotropy of the light absorption.

3.3 Conclusions

In summary, under the conditions investigated, photoelectrochemical deposition utilizing linearly polarized illumination has been shown to result spontaneously in an ordered nanoscale lamellar morphology, regardless of the wavelength distribution of the illumination source. Fourier analysis demonstrated that this morphology was consistently described by only a single periodicity. Utilization of several illumination profiles with different bandwidths but having a common intensity-weighted average wavelength resulted in structures that had a mutually common, singular periodicity. Similarly, illumination profiles that consisted of two narrowband sources generated structures that had singular periodicities which were a function of the relative contribution of each source to the total illumination intensity. Simulation of the growth process with such illumination spectral profiles showed that this phenomenon could be described by considering only the fundamental light-matter interactions that govern the photoelectrochemical growth process. Further simulations of light absorption under the same illumination profiles indicated that the photoelectrodeposition process is consistent with a self-optimization process that maximizes the anisotropy of light absorption in the structure along the growth front.